Thin Solid Films 562 (2014) 554–560

Contents lists available at ScienceDirect

Thin Solid Films

journal homepage: www.elsevier.com/locate/tsf

Three ranges of the angular dependence of critical current of $BaZrO_3$ doped $YBa_2Cu_3O_{7-\delta}$ thin films grown at different temperatures

M. Malmivirta [a,*], L.D. Yao [b], H. Huhtinen [a], H. Palonen [a,c], S. van Dijken [b], P. Paturi [a]

[a] Wihuri Physical Laboratory, Department of Physics and Astronomy, University of Turku, FI-20014 Turku, Finland
[b] NanoSpin, Department of Applied Physics, Aalto University, School of Science, P.O. Box 15100, FI-00076 Aalto, Finland
[c] The National Doctoral Programme in Nanoscience (NGS-NANO), Turku, Finland

ARTICLE INFO

Article history:
Received 10 October 2013
Received in revised form 28 April 2014
Accepted 30 April 2014
Available online 14 May 2014

Keywords:
High-temperature superconductor
Yttrium barium copper oxide
Barium zirconate
Thin films
Transmission electron microscopy
Flux pinning
Columnar defects

ABSTRACT

The growth of $BaZrO_3$ (BZO) in pulsed laser deposited $YBa_2Cu_3O_{7-\delta}$ (YBCO) thin films was studied by varying the deposition temperature. It was found that there are three deposition temperature ranges based on the properties of $J_c(\theta)$, the angular dependence of critical current density. Samples made at a relatively low temperature (low-T samples) do not show a *c*-axis peak in $J_c(\theta)$ whereas mid-T samples exhibit a peak as *B* *c*-axis of YBCO. In high-T samples the *c*-peak disappears again. In the low-T samples BZO rods are too splayed and short for a *c*-axis peak whereas in the high-T samples vortices move along correlated, but shortened rods as well as along stacking faults, which causes the *c*-axis peak to disappear. The superconducting properties of the films were studied with both magnetic and transport measurements and the structural properties were characterized using X-ray diffraction and transmission electron microscopy. Correlations between the structural and superconducting properties were analyzed using the vortex path model.

1. Introduction

The properties of $YBa_2Cu_3O_{7-\delta}$ (YBCO) thin films have been improved in the past years by many methods [1]. The most used way is to dope YBCO with a non-superconducting second phase, *e.g.* $BaZrO_3$ (BZO) [2–4], which forms either nanodots or nanorods in the YBCO matrix. In addition to increasing the critical current absolute values, BZO nanorods also affect the angular dependence of critical current, $J_c(\theta)$, where usually a broad peak is seen [4] when *B* *c*-axis of YBCO. It has been noted that while the density of rods changes with different doping concentrations, the radius of the rods stays about the same [5]. Also, it has been estimated that the rods that form do not consist entirely of BZO, but about half of rod volume contains distorted YBCO [6] and the rod is surrounded by distorted YBCO with dislocations [7]. On the other hand, in a study by Maiorov et al. [8] it was found that the rods consist merely of BZO in BZO and Y_2O_3 co-doped YBCO. The lattice mismatch between YBCO and BZO is about 9% which explains the strain and distortion of the YBCO–BZO-lattice. The strain also gives a plausible explanation for the columnar growth of BZO [9]. In a similar way, the growth of InAs columns on GaAs(100)-surface has been attributed to differences in lattice parameters [10].

The effect of deposition temperature on pulsed laser deposited (PLD) YBCO films has been studied before. In undoped YBCO, the stacking fault densities increase with deposition temperature [11], which enhances the critical current densities in a magnetic field. Also, other defect-related effects and possibly a Ba–Cu–O liquid phase during growth has been attributed to growth temperature [12]. In the latter case, an abrupt change of the shape of $J_c(\theta)$ and a drop of J_c near *ab*-peak were seen with increasing deposition temperature. The effects in BZO doped films provide similar kind of pinning improvements. The lengthening of the plateau region in $J_c(B)$-curves and the shift of the flux pinning force density maximum to higher fields with elevated deposition temperature have been attributed to correlated pinning centers [13,14]. Within the deposition temperature window used in Refs. [8] and [9] the length of the rod has been seen to increase and splay has been found to decrease with increasing deposition temperature both for BZO and BZO and Y_2O_3 co-doped YBCO. The deposition temperature does not only affect the structure but also the growth mode of pure YBCO; low substrate temperatures produce spiral growth while at higher temperatures (normal conditions) 2D nucleation and growth is favored during pulsed laser deposition [15].

In this paper, we study the effect of growth temperature in BZO doped PLD YBCO thin films. The film structures were characterized with X-ray diffraction and transmission electron microscopy (TEM). The superconducting properties were determined using

* Corresponding author.
E-mail address: mika.malmivirta@utu.fi (M. Malmivirta).

http://dx.doi.org/10.1016/j.tsf.2014.04.093
0040-6090/

magnetic measurements and also the angular dependencies of critical currents were measured. The results are interpreted with the vortex path model for angular dependencies of critical currents. The structural results are connected to the superconducting properties.

2. Experimental details

The films were grown with a pulsed laser deposition (PLD) system on 5×5 mm^2 $SrTiO_3$ (100) substrates using a 5 wt.% BZO doped nanostructured YBCO target (prepared as described in [16]). The deposition system is described in more detail in [17]. The deposition temperature T_{dep} was varied between 700 and 850 °C in 25 °C steps and after ablation each film was oxygenated at 50 °C below T_{dep} in an atmospheric pressure of O_2 for 10 min. Ablation was done with a XeCl excimer laser ($\lambda = 308$ nm) in an oxygen pressure of 23 Pa. Based on the properties of the $J_c(\theta)$ curves of the films, they were grouped into three categories: low-, mid- and high-T groups where T refers to deposition temperature. The boundary between low- and mid-T categories is about 700–725 °C and between mid- and high-T is about 800–825 °C. In each category, several films were made with different deposition temperatures. Because there are no major differences between the films in the same category, the properties of mainly one film is presented from each group.

The crystal structures were examined with an X-ray diffractometer (Philips X'pert Pro with Schulz texture goniometer). To check the purity of the films, θ–2θ scans with $\psi = 0$ were measured between 20° and 70°. Also, more accurate θ–2θ and rocking curve scans were performed on the YBCO (005) peak. To determine the growth of BZO, similar θ–2θ and rocking curve scans were made for BZO (002). The crystal growth direction was determined by 2θ–ϕ scans for YBCO (102) with two different ψ for *c*- and *a*-axis oriented grains. Similar 2θ–ϕ scans were taken of YBCO (212) to quantify twinning [18]. In addition to this, a 2θ–ϕ scan for BZO (110) was made. The microstructure of the films was analyzed by electron transmission microscopy using a JEOL 2200FS TEM instrument with double Cs correctors, operated at 200 keV. All cross-sectional TEM specimens were prepared by a modified mechanical polishing method; a Si/film/Si sandwich structure was firstly glued by epoxy after which it was cut into thin slices. After that, the thin slices were ground and polished by a MultiPrep polishing system (Allied High Tech products, Inc.), and finally milled in an Ar ion polishing system (Model 691 PIPS, Gatan Inc.).

The magnetic and superconducting properties were determined with a Quantum Design Physical Property Measurement System (PPMS). The onset critical temperature T_c was defined with the ACMS option of the PPMS from the onset temperature of the in-phase component of the AC-magnetization. DC-magnetization was measured between −8 and 8 T at 10 and 77 K and from these measurements the critical current was calculated using the Bean formula [19]. The angular dependencies of the critical currents were measured using the horizontal rotator option in magnetic fields between 0.5 and 8 T and at angles between 0° and 360° in the maximum Lorentz force configuration using 3° steps. For these measurements, each sample was patterned with wet chemical etching. The etched pattern was a standard four probe measurement circuit with a 50 μm wide current stripe. The contacts on the samples were made by tapping with indium. Measurements were done at temperatures 10–70 K in 10 K steps for all fields and angles. The values for voltage between the voltage pads as a function of applied current were recorded with the critical electric field of 215 μV/cm. On some samples the critical value was increased slightly to deal with the noise. However, the shape of the $J_c(\theta)$-curve did not change with the voltage limit [20].

3. Results and discussion

3.1. Structural properties

By scanning the YBCO (102) peak in *a*- and *c*-axis configurations, it was assured that there were no *a*-axis oriented grains in any of the samples. In scans of the YBCO (212) peak set, peak splits due to twinning are clearly seen for high-T samples and slightly less clearly in the other group, but the width of the four peak set stays approximately constant in 2θ- and ϕ-directions throughout different deposition temperatures. The splits in high-T films indicate that the structure of high-T samples is slightly more relaxed than that of the low- and mid-T samples. Rocking curves of YBCO (005) showed full width at half maximum (FWHM) values of 0.2°–0.3° with no clear dependence on deposition temperature. The values are similar to what has been found before [21,14]. According to these results, the YBCO matrix does not contain out-of-plane oriented grains. Also the oxygen content of YBCO lattice was estimated by comparing the intensities of (00*l*) YBCO peaks in θ–2θ-diffractograms. $I(005)/I(004) < 20$ and $I(005)/I(007)$ is between 7 and 10, and thus $\delta < 0.1$ [22] for all films.

BZO, on the other hand, shows a stronger dependence on T_{dep}. The evolution of its (002)-peak as a function of T_{dep} (Fig. 1) clearly shows a change of the BZO lattice parameters with T_{dep}. At low temperatures the peak is seen at a higher 2θ angle than the corresponding peak of a bulk sample (vertical line in figure is calculated from data in [23]). At higher temperatures another peak forms at lower 2θ angle, close to the bulk value. In other words, with increasing deposition temperature the *c*-axis parameter rises from smaller than bulk to about the same as bulk. A similar evolution is found for BZO (110), *i.e.* a peak also shifts to lower 2θ values with higher T_{dep}. Due to the small amount of BZO in the YBCO matrix, the diffractograms are too noisy that the differences in the FWHMs of the curves could reliably be seen.

Cross-sectional TEM images of low-, mid- and high-T samples (Fig. 2) show significant differences in the films. In the low-T sample there are splayed nanocolumns with a width of 4.5–5.5 nm and a splaying angle of about 15°–30° with respect to the *c*-axis. In the mid-T sample there are well-aligned rods with a width of 6–7 nm. According to this image, the rods are separated by about 10–15 nm. The high-T sample has equally aligned nanocolumns with a width of 4–8 nm, but they are shorter than in the mid-T sample. Also, a large number of stacking faults parallel to the *ab*-plane are observed. The rod diameters have in all the cases been extracted from a single image and they may not always be representative samples. Therefore, it cannot be said that the rod diameters in different temperature ranges would differ significantly. According to energy dispersive X-ray spectroscopy, the rods in all the samples do not consist merely of BZO but

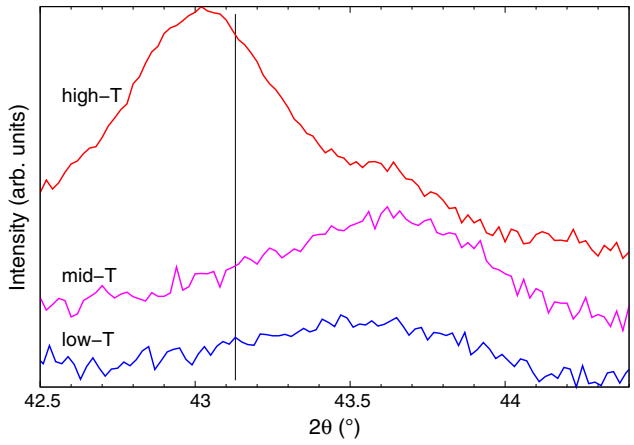

Fig. 1. The evolution of BZO (002) peak with deposition temperature. The black vertical line shows the 2θ-value of bulk BZO. The intensities have been shifted for readability.

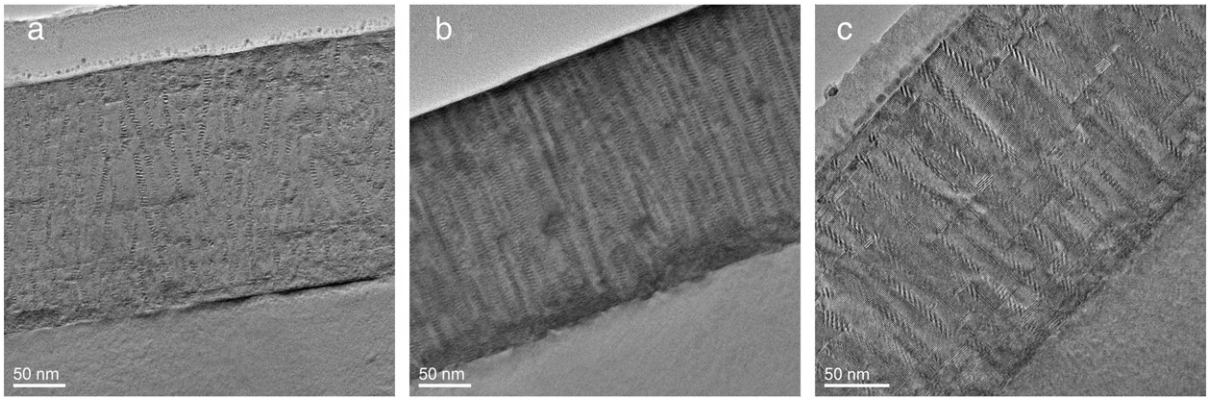

Fig. 2. Cross-sectional TEM images of (a) low-T, (b) mid-T and (c) high-T films.

incorporate also Y and Cu atoms. Moreover, the nanocolumns contrast in all samples seemingly corresponds to Moire fringes between YBCO and BZO nanorods, which is in agreement with the previous reports [6,8].

In all the samples, BZO has a large interface area in the YBCO matrix. To relieve the interfacial strain, BZO shortens its lattice parameters and thus larger 2θ values than in the bulk are attained. Moreover, the extra Y and Cu atoms in the BZO rods cause an additional distortion of the BZO lattice parameters. On the other hand, in the high-T sample the peak at smaller 2θ value in the diffractogram (Fig. 1) corresponds to pure BZO phase. The double peak indicates that BZO is more pure in the high-T than in other samples and this is possible because BZO hardly reacts with YBCO [24].

3.2. Magnetic properties

The magnetically determined onset critical temperatures increase monotonically from 80 K *via* 85 K in the mid-T samples to almost 90 K in the high-T samples (Fig. 3a inset). At the same time, the width of the transition decreases from approximately 10 K in low-T films to 2–3 K in mid-T films. In high-T films the width starts to increase again being around 8 K at the highest deposition temperature of 850 °C. The rise of T_c and eventually a small decrease with deposition temperature are similar to the observations by Galluzzi et al. [13] for 7% BZO doped films. Also in our work the film quality decreases with too high deposition temperature. As can be seen in our TEM images, the decrease of quality could be explained by the increasing amount of stacking faults while the oxygen content stays the same.

The magnetically determined critical current density at 10 K and 0 T (Fig. 3a) depends similarly on T_{dep} as T_c. At first the value of J_c rises to about 30–40 MA/cm^2 and deteriorates again at high deposition temperatures. The increase is likely to be caused by better pinning on more ordered BZO columns and better superconductivity between the rods. In the high-T sample, stacking faults start to deteriorate pinning. Also, the shape of the $J_c(T_{dep})$ curve in nonzero magnetic field does not differ from this curve significantly. At 77 K and 0 T the J_c dependence on magnetic field reflects both T_c and the width of the transition. Before this work, a monotonic increase of J_c with deposition temperature has been found for BZO doped YBCO in moderate fields [9]. On the other hand, BZO and Y_2O_2 co-doped YBCO showed a maximum of J_c at 800 °C in a study by Maiorov et al. [8]. For undoped YBCO both a maximum [12] and a monotonic increase [11] of J_c has been found.

The accommodation field B^* for which $J_c(B^*) = 0.9J_c(0)$ at 10 K (Fig. 3b) approximately linearly decreases from 400 mT (T_{dep} = 700 °C) to 100 mT (T_{dep} = 850 °C). At 77 K, B^* shows a quite opposite trend with deposition temperature and the magnitude of B^* is remarkably smaller than that at 10 K. It is noteworthy that in the case of BZO doped samples, $B^* < B_\phi$ [25], where B_ϕ is the so called matching field, where there is one pinning site per vortex. At B^*, the pinning changes from the single to the collective vortex pinning regime [26]. In other words, the decrease of B^* means that pinning in small fields and at low temperatures is deteriorated as T_{dep} is increased. This can be explained by the fact that in the low-T samples there are more but shorter and more splayed rods. The rods pin vortices at sites that minimizes vortex–vortex interaction. In mid- and high-T samples the number of vortices in such optimal places is smaller because straighter rods force vortices to sit more precisely at certain points. The straighter rods, however, are responsible for the increase of J_c at 0 T. At 77 K, on the other hand, B^* reflects mainly the behavior of T_c.

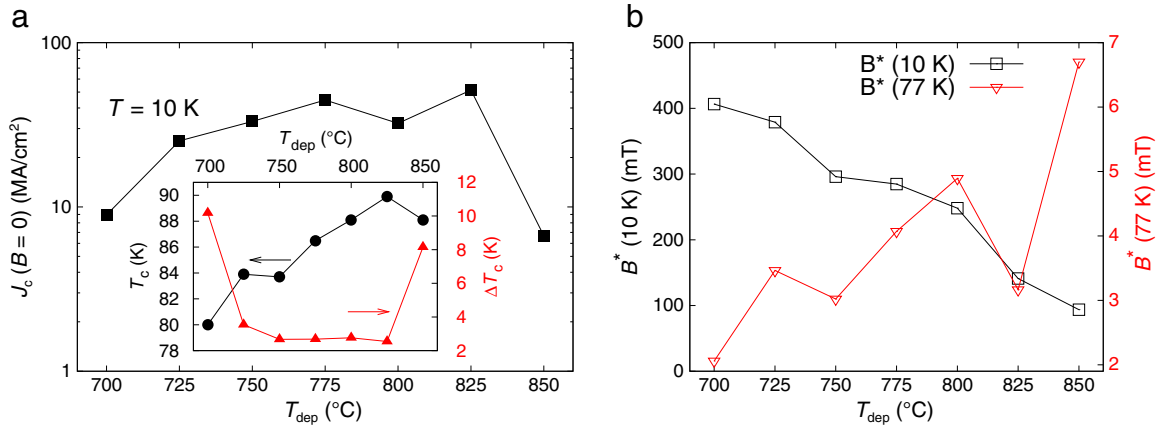

Fig. 3. (a) Critical current density at 10 K as a function of deposition temperature and the evolution of the onset temperature and the width of the transition (inset). (b) The accommodation field of samples at 10 K and at 77 K.

The critical current exponent α at 10 K ($J_c \propto B^{-\alpha}$) is about 0.35 for the low- and high-T samples and about 0.15–0.20 for mid-T samples. That is to say, the pinning properties in magnetic field are the best in themed-T samples. In Ginzburg–Landau simulations [27] the smallest α was achieved with the largest rod diameter. In this experimental case, however, the $J_c(B)$ is less linear at $B > B^*$ than in simulations and the widths of the rods are not all the same. Because no clear differences between the rod diameters are seen in TEM images (Fig. 2), there must be also other pinning mechanisms that can affect the value of α. At 77 K, the values of α are somewhat larger, about 0.35–0.50 for low- and high-T films and 0.25–0.35 for mid-T films. It is interesting to see that mutually inconsistent results have been found previously for the temperature dependence of the rod diameter. In a study by Baca et al. [9], the diameter of the rods was not seen to change with deposition temperature, whereas $SmBa_2Cu_3O_y$ doped with BZO [28] showed a clear increase in rod diameter with increased deposition temperature.

3.3. Angular dependence of critical current

Below T_c ($\lesssim$70 K), the shape of the angular dependence of the critical current is roughly constant at different measurement temperatures. This is also the case for the magnetic field dependencies of J_c [5,29] as J_c drops almost linearly with rising measurement temperature. The measurements of angular dependencies of critical current, I_c, are shown for the three deposition temperature ranges in Fig. 4a–c. The $\theta = 0°$ corresponds to the case where B c-axis of YBCO. Although the measurements were made in a rather wide temperature range, only the measurements at 40 K are shown, since it is far enough from T_c and technologically more important than 10 K [30]. The angular dependencies of critical currents in films of different deposition temperatures exhibit major changes with increasing deposition temperature. Going from low-T to mid-T films, the c-axis peak appears. When going even further to the high-T range the c-axis peak disappears again. This is intuitively related to the continuous rods seen in the TEM-image of the mid-T sample. Splayed and shorter columns in the low-T sample and shorter columns and stacking faults in the high-T sample both result in the disappearance of the c-axis peak. The twin boundaries and dislocations present in all the samples are not strong enough to create the c-axis peak.

Between the low- and mid-T ranges the c-axis peak appears first at high magnetic fields as a double peak *i.e.* two peaks near $\theta = 0°$ (Fig. 5). Going to mid-T, the peak evolves to a single and sharper peak and eventually disappears in films deposited at high enough temperature. At 0.5 T there is no c-axis peak seen in any of the $J_c(\theta)$-curves. Baca et al. [9] have found a c-peak at 1 T and 77 K for BZO doped samples whereas in this work the c-axis peak is seen more clearly only at higher fields but for all measurement temperatures. At fields higher than the matching field B_ϕ, the c-peak should disappear at higher measurement temperatures [25]. Calculating the defect density from the distance between nanorods in the TEM image of the mid-T film (15 nm) and assuming a square lattice, we estimate a rod density of approximately 4400 μm^{-2}. Using the formula $B_\phi = n\Phi_0$, where Φ_0 is the flux quantum and n is the density of defects, this gives $B_\phi \approx 92$ T. Therefore, the c-axis peak should not disappear in the measurement fields used in this study.

The ab-peak also changes drastically with T_{dep}. The shape of the curve for the low-T film is approximately independent of B. For mid-T

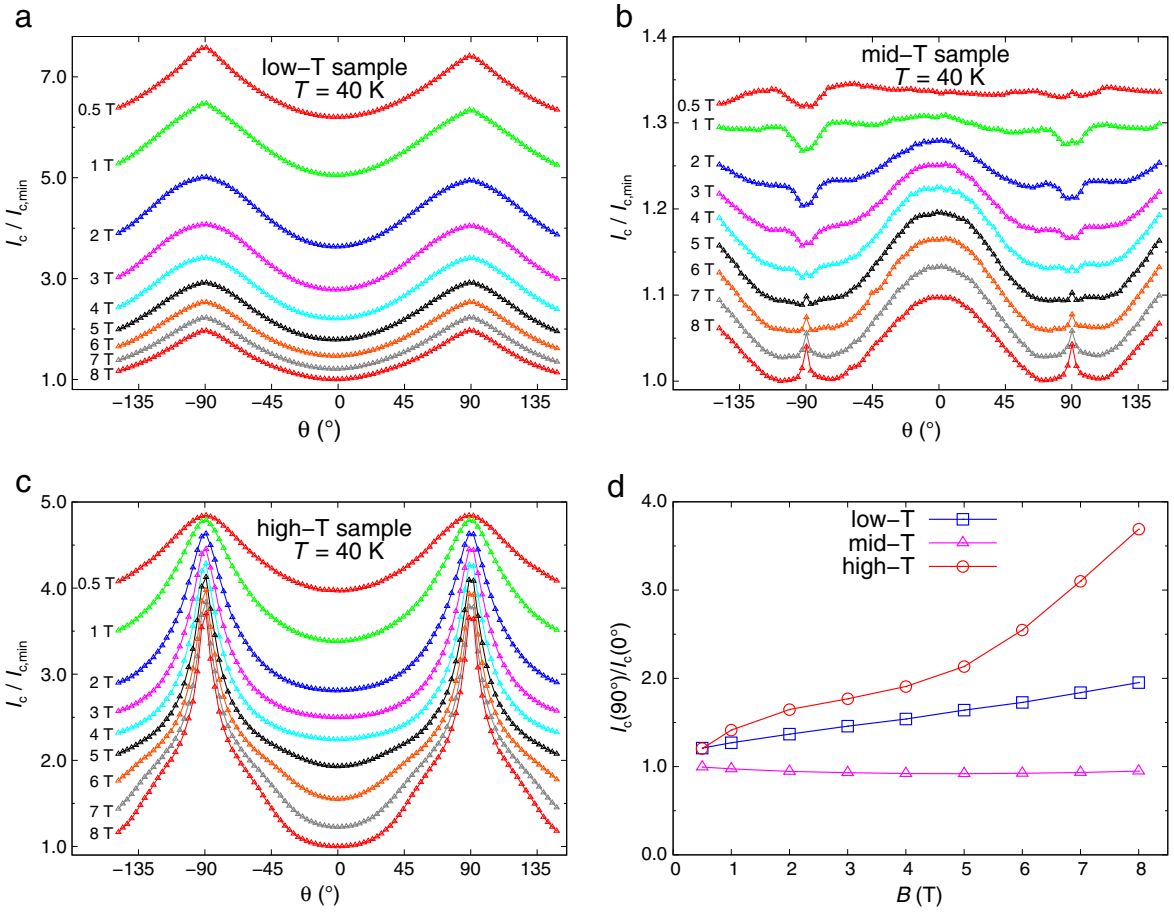

Fig. 4. The angular dependencies of critical current I_c in low-T (a), mid-T (b) and high-T (c) films in different magnetic fields. The I_c-values are scaled with the minimum of I_c at 8 T. (d) The relative values of ab-peak to c-peak show a clear dependence on the deposition temperature. There are no large differences between measurements at different temperatures far from T_c. As an example, the measurements made at 40 K are shown.

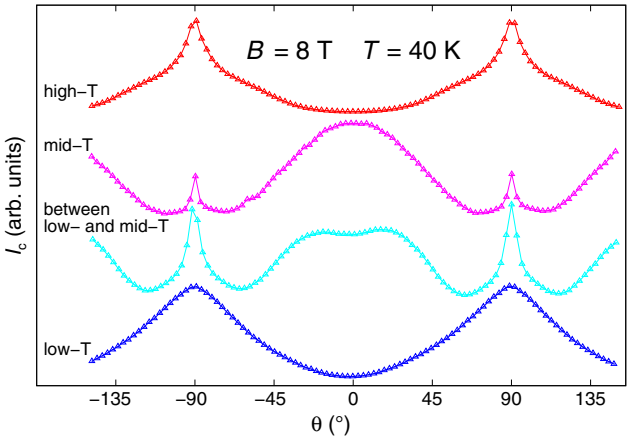

Fig. 5. The evolution of the *c*-axis peak in different temperature ranges. The curves have been normalized and shifted for clarity.

and low *B*, the *ab*-peak first forms a dip and then evolves into a sharp peak with increasing magnetic field. For the high-T sample, the *ab*-peak does not disappear and it sharpens at higher fields. Wang et al. [29] explained that the more ordered rods, which are attained with higher deposition temperature, distort the *ab*-planes of YBCO and thus deteriorate pinning in that direction. In our experiments, this corresponds to the samples between the low- and mid-T ranges. At higher deposition temperature, the pinning in the *ab*-direction is enhanced. This can be explained by the large number of stacking faults, which are clearly visible in the TEM image of Fig. 2c.

There is a major change in the ratio $I_c(B\,ab)/I_c(B\,c)$ (Fig. 4d) with deposition temperature. The ratio reflects the anisotropy of the sample. If this value becomes closer to one, the anisotropy decreases. The mid-T sample has much smaller anisotropy than the other films, and for that film the ratio described above does not show a clear dependence on magnetic field either. With increasing field the critical current drops only 22% in the *ab*-direction and 18% in the *c*-direction as *B* changes from 0.5 T to 8 T. Thus, the ratio plotted in Fig. 4d does not change significantly for the mid-T range.

For the other two ranges, the change in anisotropy is much larger. The drop of I_c in the low-T sample is about 80% with field and it stays roughly the same through all angles. In the high-T sample the drop is much greater in the *c*-direction (75%) than in the *ab*-direction (23%) and thus the relative difference in the critical values becomes larger. The value of $I_c(B\,ab)/I_c(B\,c)$ in the low-T sample rises due to the diminished critical current whereas the shape of the curve stays almost the same. In practice, there are less *c*-oriented pinning sites in both the low- and high-T samples than in the mid-T samples. The shattered and, in the sense of pinning, too splayed rods are not equally good for pinning in the *c*-direction. Although in both low- and high-T films the ratio $I_c(B\,ab)/I_c(B\,c)$ is large, there are clear differences in the nature of the pinning sites for the low- and high-T films as indicated by the TEM-images and the dissimilar angular dependencies of J_c.

The change in T_{dep} where the *c*-axis peak appears is rather small. Wang et al. [29] used two films with 20 °C difference in deposition temperature and their lower-T film did not have a *c*-peak while the higher one did. The rods that form have been noted to be more continuous with increasing T_{dep} by Baca et al. [9] and by Maiorov et al. [8] within a narrower temperature window than used in this work. Also, according to Baca et al., BZO forms less nanoparticles and more continuous rods with higher deposition temperature. This behavior is confirmed by our experiments, with the exception of high-T samples where the rods start again to be more discontinuous.

As the length of the rod decreases with decreasing deposition temperature, at some point we go over the limit that BZO rods are no longer correlated rods but roughly spherical pinning centers. In that case, they do not exhibit a *c*-axis peak [31]. As pointed out by Maiorov et al. [8], the pinning sites are still stronger than mere point pinning centers. Considering growth kinetics, the reason for the disappearance of the *c*-peak in low-T sample could be related to a maximum in the formation probability as a function of T_{dep}. That would also explain the discontinuous columns in the high-T range. This initial idea on strain-mediated growth as postulated by Xie et al. [10] was further developed for BZO doped YBCO by Baca et al. [9].

To quantify the change of the *c*-axis peak in the angular dependence of J_c, the vortex path model [32–35] was fitted to the 40 K data. In short, the model treats vortices at pinning sites statistically. Depending on the steps that vortices take inside the superconductor, there either exists or does not exist a *c*-peak. The practical realization of the model is similar to that described in [32]. The overall critical current density is divided into three parts

$$J_{c,\mathrm{tot}}(\theta) = J_c(\theta) + J_c(\theta + 90^\circ) + J_{c,\mathrm{rand}}(\theta). \tag{1}$$

In the Eq. (1) above,

$$J_c(\theta) = J_0\left[\frac{1-\eta}{\sin^2(\theta)}\exp\left(-\frac{1}{2\Gamma_G^2\tan^2(\theta)}\right) + \frac{\eta}{\cos^2(\theta)+\Gamma_L^2\sin^2(\theta)}\right], \tag{2}$$

where θ is the deviation from *c*-axis, η is the Lorentzianity of the peak, Γ_L and Γ_G are parameters giving the width of the Lorentzian and Gaussian peak shapes and J_0 is a scaling constant. For the *ab*-peak, $\eta = 1$ and only the Lorentzian part is considered. For the *c*-peak in $J_c(\theta)$, θ shifted by 90°. The random part above is taken as [32,36]

$$J_{c,\mathrm{rand}}(\theta) = J_{c,0}\left(\cos^2(\theta) + \sin^2(\theta)/\gamma^2\right)^{-1/2}. \tag{3}$$

Again, $J_{c,0}$ is a scaling constant and γ is the effective mass anisotropy parameter for which a value of 3.4 was used for BZO doped films [17]. The parameter γ is constant in the function that transforms a physical quantity from anisotropic to isotropic systems. The larger γ is, the larger is the anisotropy of the system. The scaling of random pinning centers with electron mass anisotropy was developed by Blatter et al. [36].

An example fit to the data from a high-T sample at 40 K and 8 T with different components is shown in Fig. 6. From the fitted parameters the FWHM for the *c*-axis peak using the formula from [32] was calculated. A clear difference in FWHMs is seen, depending on whether there is a *c*-peak or not (Fig. 7). Films that show a *c*-axis peak, have FWHM $\lesssim 55°$ and without a *c*-peak they have FWHM $\gtrsim 55°$. With highest T_{dep} before the disappearance of the *c*-peak, the FWHM is narrowed down

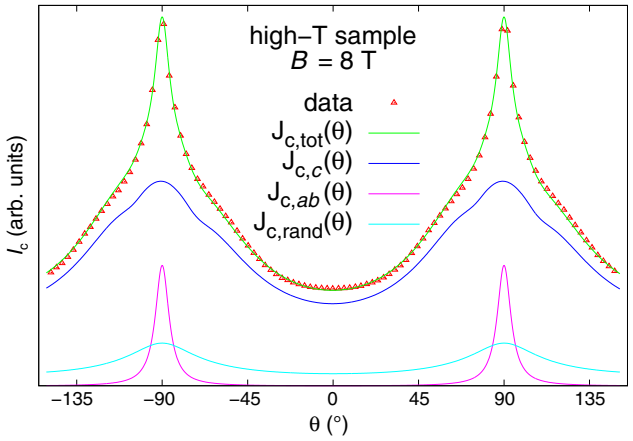

Fig. 6. The vortex path model fitted to the high-T sample data taken at 40 K and 8 T. The actual fit $J_{c,\mathrm{tot}}$ consists of a part giving the *ab* peak ($J_{c,ab}$) and the *c*-peak ($J_{c,c}$). The random point pinning part added is ($J_{c,\mathrm{rand}}$). In this particular example, there is no *c*-peak, but shoulders near *ab*-peak.

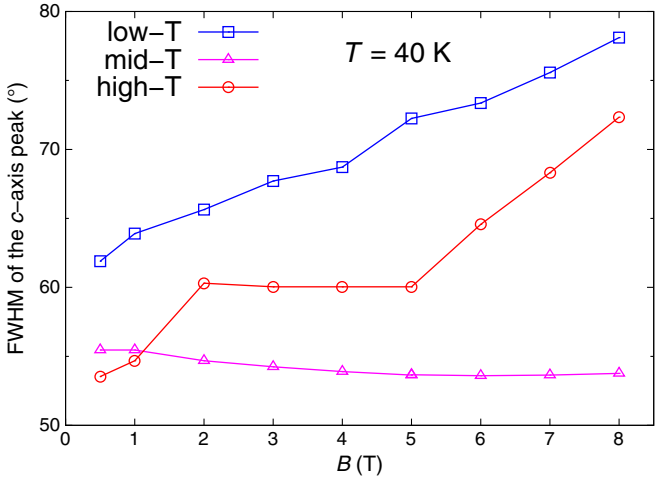

Fig. 7. The FWHM of the *c*-axis peak in $J_c(\theta)$-figure in different deposition temperature ranges determined by fitting the vortex path model to the data. Only mid-T films have a *c*-peak and it is also reflected to this figure.

to 45° in 8 T as the field is increased whereas the FWHM stays nearly constant at lower deposition temperatures that show the peak (mid-T in Fig. 7). For the films without a *c*-peak the whole shape of the FWHM(B) changes. In many of these cases, the pseudo-Voigt distribution width Γ is large enough so that no *c*-axis peak is seen. Instead, a contribution near or at the *ab*-peak [32,33] is observed, depending on whether Γ_G or Γ_L is large. In general, the values of Γ are similar to the values reached before, but the FWHM is slightly decreased with increasing field, which is opposite to [32]. However, the BZO doped film in [32] was deposited at temperature between low- and mid-T ranges and the decrease is strongest at T_{dep} which is near the transition between mid- and high-T ranges.

The fitted pseudo-Voigt width Γ (or since peaks are mostly Lorentzian, Γ_L) is related to the vortex steps by [32,33]

$$\Gamma = \frac{\sigma}{\sqrt{m}\lambda}, \tag{4}$$

where σ is the standard deviation of the distances of columnar pinning sites, m is the average number of steps that vortices take and λ is the average length of a step at a pinning site. In the *c*-direction, $m\lambda$ equals the thickness of the film. The standard deviation of the distance distribution of the rods $\sigma = 34$ nm was taken from [32]. The standard deviation σ is according to Eq. (4) proportional to Γ and thus σ would likely be the smallest for samples with the smallest Γ.

To give an illustrative picture of the vortex steps, the step length and number of steps were calculated from Eq. (4). The calculated results are shown in Table 1 for averages of Γ in different magnetic fields. The 700 °C sample is in the low-T range, 725–800 °C in the mid-T range and 825 °C in the high-T range. For samples with small splay and long rods (mid-T) one gets the smallest Γ and thus the largest step lengths, about 45 nm as a maximum. Also the number of steps shows a minimum in this case. In the low- and high-T samples without a *c*-peak, vortices take more steps and the steps are consequently shorter. Although high-T samples have correlated pinning centers, no *c*-axis peak is seen. Vortices follow both the rods and the stacking faults that can be seen in the TEM images. In other words, the absence of the *c*-axis peak does not necessarily imply that there would not be any correlated pinning centers.

Table 1
Vortex path step length λ with different deposition temperatures. Γ_L is the Lorentzian width of the curve and m the number of steps.

T_{dep} (°C)	Γ_L	m	λ (nm)
700	1.2	8	19.5
725	1.0	5	32.2
775	0.9	3	44.9
800	0.9	3	43.6
825	1.1	8	21.8

4. Conclusions

BZO doped YBCO thin films were grown by PLD at different deposition temperatures (T_{dep}). With higher T_{dep} straighter rods were formed and also the number of stacking faults increased. Three temperature ranges were identified, and only in the mid-T range the films exhibit a peak in $J_c(\theta)$ when B *c*-axis of YBCO. Low-T films have too splayed rods for a *c*-axis peak to appear and the stacking faults in high-T films prevent the appearance of a *c*-axis peak although correlated rods exist. As is illustrated by the vortex path model, the vortices in both the low- and high-T cases take shorter steps than in the films of the mid-T range.

Acknowledgments

Jenny and Antti Wihuri Foundation and Finnish Foundation for Technology Promotion are acknowledged for financial support.

References

[1] S.R. Foltyn, L. Civale, J.L. MacManus-Driscoll, Q.X. Jia, B. Maiorov, H. Wang, M. Maley, Materials science challenges for high-temperature superconducting wire, Nat. Mater. 6 (2007) 631.
[2] H. Yamada, H. Yamasaki, K. Develos-Bagarinao, Y. Nakagawa, Y. Mawatari, J.C. Nie, H. Obara, S. Kosaka, Flux pinning properties of *c*-axis correlated pinning centres in PLD-YBCO films, Supercond. Sci. Technol. 17 (2004) S25.
[3] J.L. MacManus-Driscoll, S.R. Foltyn, Q.X. Jia, H. Wang, A. Serquis, L. Civale, B. Maiorov, M.E. Hawley, M.P. Maley, D.E. Peterson, Strongly enhanced current densities in superconducting coated conductors of $YBa_2Cu_3O_{7-x}$ + $BaZrO_3$, Nat. Mater. 3 (2004) 439.
[4] A. Goyal, S. Kang, K.J. Leonard, P.M. Martin, A.A. Gapud, M. Varela, M. Paranthaman, A.O. Ijadoula, E.D. Specht, J.R. Thompson, D.K. Christen, S.J. Pennycook, F.A. List, Irradiation free, columnar defects comprised of self-assembled nanodots and nanorods resulting in strongly enhanced flux pinning in $YBa_2Cu_3O_{7-\delta}$ films, Supercond. Sci. Technol. 18 (2005) 1533.
[5] P. Paturi, M. Irjala, H. Huhtinen, A.B. Abrahamsen, Modeling flux pinning in thin undoped and $BaZrO_3$-doped YBCO films, J. Appl. Phys. 105 (2009) 023904.
[6] M. Peurla, H. Huhtinen, M.A. Shakhov, K. Traito, Y.P. Stepanov, M. Safonchik, P. Paturi, Y.Y. Tse, R. Palai, R. Laiho, Effects of nanocrystalline target and columnar defects on flux pinning in pure and BZO-doped YBCO films in fields up to 30 T, Phys. Rev. B 75 (2007) 184524.
[7] M. Peurla, H. Huhtinen, Y.Y. Tse, J. Raittila, P. Paturi, Structural properties of YBCO thin films deposited from different kinds of targets, IEEE Trans. Appl. Supercond. 17 (2007) 3608.
[8] B. Maiorov, S.A. Baily, H. Zhou, O. Ugurlu, J.A. Kennison, P.C. Dowden, T.G. Holesinger, S.R. Foltyn, L. Civale, Synergetic combination of different types of defect to optimize pinning landscape using $BaZrO_3$-doped $YBa_2Cu_3O_7$, Nat. Mater. 8 (2009) 398.
[9] F.J. Baca, T.J. Haugan, P.N. Barnes, T.G. Holesinger, B. Maiorov, R. Lu, X. Wang, J.N. Reichart, J.Z. Wu, Interactive growth effects of rare-earth nanoparticles on nanorod formation in $YBa_2Cu_3O_x$ thin films, Adv. Funct. Mater. 23 (2013) 4826.
[10] Q. Xie, A. Madhukar, P. Chen, N.P. Kobayashi, Vertically self-organized InAs quantum box islands on GaAs(100), Phys. Rev. Lett. 75 (1995) 2542.
[11] J. Wang, J.H. Kwon, J. Yoon, H. Wang, T.J. Haugan, F.J. Baca, N.A. Pierce, P.N. Barnes, Flux pinning in $YBa_2Cu_3O_{7-\delta}$ thin film samples linked to stacking fault density, Appl. Phys. Lett. 92 (2008) 082507.
[12] D.M. Feldmann, O. Ugurlu, B. Maiorov, L. Stan, T.G. Holesinger, L. Civale, S.R. Foltyn, Q.X. Jia, Influence of growth temperature on critical current and magnetic flux pinning structures in $YBa_2Cu_3O_{7-x}$, Appl. Phys. Lett. 91 (2007) 162501.
[13] V. Galluzzi, A. Augieri, T. Petrisor, L. Ciontea, G. Celentano, A. Mancini, A. Vannozzi, A. Angrisani, A. Rufoloni, Deposition and characterization of YBCO films with BZO inclusions on single crystal substrate, Physica C 470 (2010) S142.
[14] A. Augieri, V. Galluzzi, G. Celentano, A.A. Angrisani, A. Mancini, A. Rufoloni, A. Vannozzi, E. Silva, N. Pompeo, T. Petrisor, L. Ciontea, U. Gambardella, S. Rubanov, Transport property improvement by means of BZO inclusions in PLD grown YBCO thin films, IEEE Trans. Appl. Supercond. 19 (2009) 3399.
[15] B. Dam, N.J. Koeman, J.H. Rector, B. Stäuble-Pümpin, U. Poppe, R. Griessen, Growth and etching phenomena observed by STM/AFM on pulsed-laser deposited $YBa_2Cu_3O_{7-\delta}$ films, Physica C 261 (1996) 1.
[16] J. Raittila, H. Huhtinen, P. Paturi, Y.P. Stepanov, Preparation of superconducting $YBa_2Cu_3O_{7-\delta}$ nanopowder by deoxydation in Ar before final oxygenation, Physica C 371 (2002) 90.

[17] H. Palonen, H. Huhtinen, M.A. Shakhov, P. Paturi, Electron mass anisotropy of $BaZrO_3$ doped YBCO thin films in pulsed magnetic fields up to 30 T, Supercond. Sci. Technol. 26 (2013) 045003.
[18] P. Paturi, M. Peurla, K. Nilsson, J. Raittila, Crystalline orientation and twin formation in YBCO thin films laser ablated from a nanocrystalline target, Supercond. Sci. Technol. 17 (2004) 564.
[19] H.P. Wiesinger, F.M. Sauerzopf, H.W. Weber, On the calculation of J_c from magnetization measurements on superconductors, Physica C 203 (1992) 121.
[20] J.H. Durrell, D.M. Feldmann, C. Cantoni, Suppression of vortex channeling in meandered YBCO grain boundaries, Appl. Phys. Lett. 91 (2007) 182506.
[21] H. Huhtinen, K. Schlesier, P. Paturi, Growth and c-axis flux pinning of nanostructured YBCO/BZO multilayers, Supercond. Sci. Technol. 22 (2009) 075019.
[22] J. Ye, K. Nakamura, Quantitative structure analyses of $YBa_2Cu_3O_{7-\delta}$ thin films: determination of oxygen content from X-ray-diffraction patterns, Phys. Rev. B 48 (1993) 7554.
[23] I. Levin, T.G. Amos, S.M. Bell, L. Farber, T.A. Vanderah, R.S. Roth, B.H. Toby, Phase equilibria, crystal structures, and dielectric anomaly in the $BaZrO_3$–$CaZrO_3$ system, J. Solid State Chem. 175 (2003) 170.
[24] A. Erb, E. Walker, R. Flükiger, $BaZrO_3$: the solution for the crucible corrosion problem during the single crystal growth of high-T_c superconductors $REBa_2Cu_3O_{7-\delta}$; RE = Y, Pr, Physica C 245 (1995) 245.
[25] P. Paturi, M. Irjala, A.B. Abrahamsen, H. Huhtinen, Defining B_c, B^* and B_ϕ for YBCO Thin Films, IEEE Trans. Appl. Supercond. 19 (2009) 3431.
[26] F.C. Klaassen, G. Doornbos, J.M. Huijbregtse, R.C.F. van der Geest, B. Dam, R. Griessen, Vortex pinning by natural linear defects in thin films of $YBa_2Cu_3O_{7-\delta}$, Phys. Rev. B 64 (2001) 184523.
[27] H. Palonen, J. Jäykkä, P. Paturi, Modeling reduced field dependence of critical current density in $YBa_2Cu_3O_{6+x}$ films with nanorods, Phys. Rev. B 85 (2012) 024510.
[28] T. Ozaki, Y. Yoshida, Y. Ichino, Y. Takai, A. Ichinose, K. Matsumoto, S. Horii, M. Mukaida, Y. Takano, Flux pinning properties and microstructure of $SmBa_2Cu_3O_y$ thin films with systematically controlled $BaZrO_3$ nanorods, J. Appl. Phys. 108 (2010) 093905.
[29] X. Wang, F.J. Baca, R.L.S. Emergo, J.Z. Wu, T.J. Haugan, P.N. Barnes, Eliminating thickness dependence of critical current density in $YBa_2Cu_3O_{7-x}$ films with aligned $BaZrO_3$ nanorods, J. Appl. Phys. 108 (2010) 113911.
[30] D. Larbalestier, A. Gurevich, D.M. Feldmann, A. Polyanskii, High-T_c superconducting materials for electric power applications, Nature 414 (2001) 368.
[31] V.F. Solovyov, H.J. Wiesmann, L. Wu, Q. Li, L.D. Cooley, M. Suenaga, B. Maiorov, L. Civale, High critical currents by isotropic magnetic-flux-pinning centres in a 3 μm thick $YBa_2Cu_3O_7$ superconducting coated conductor, Supercond. Sci. Technol. 20 (2007) L20.
[32] P. Paturi, The vortex path model and angular dependence of J_c in thin YBCO films deposited from undoped and $BaZrO_3$-doped targets, Supercond. Sci. Technol. 23 (2010) 025030.
[33] N.J. Long, Model for the angular dependence of critical currents in technical superconductors, Supercond. Sci. Technol. 21 (2008) 025007.
[34] N.J. Long, N.M. Strickland, E.F. Talantsev, Modeling of vortex paths in HTS, IEEE Trans. Appl. Supercond. 17 (2007) 3684.
[35] S. Wimbush, N. Long, The interpretation of the field angle dependence of the critical current in defect-engineered superconductors, New J. Phys. 14 (2012) 083017.
[36] G. Blatter, M.V. Feigel'man, V.B. Geshkenbein, A.I. Larkin, V.M. Vinokur, Vortices in high-temperature superconductors, Rev. Mod. Phys. 66 (1994) 1125.